Rare Met. (2022) 41(8):2819–2825
https://doi.org/10.1007/s12598-021-01949-0

RARE METALS

LETTER

Embedment of red phosphorus in anthracite matrix for stable battery anode

Yu-Chen Tan, Wei-Wei Liu*, Wen-Yu Wang, Xiao-Xiao Liu, Jun-Mou Du, Yong-Ming Sun*

Received: 26 September 2021 / Revised: 29 October 2021 / Accepted: 17 November 2021 / Published online: 11 March 2022

Red phosphorus (red P) is a promising anode material for lithium-ion batteries (LIBs) due to its high theoretical capacity of 2596 mAh·g^{-1}, abundant resource and low cost. However, the application of P-based anode suffers from several crucial issues, including limited electronic conductivity and drastic volume variation during its electrochemical lithiation/delithiation processes. Here, we reported a red P/anthracite composite featuring red P embedded into micrometer-scale porous anthracite framework fabricated through a one-pot ball milling synthesis process. The micrometer-sized anthracite not only provided high electronic conductivity but also worked as buffer matrix to mitigate the volume change of the active materials during cycling. P–C and P–O–C bonds between P and anthracite enabled their close contact and thus stabilized the structure of red P/anthracite composite. Also, the one-pot synthesis operation was facile, and the raw materials of red P and anthracite were in low cost. As expected, the red P/anthracite composite showed stable electrochemical cycling and satisfied rate capability for LIBs. It delivered an overall high initial capacity of 810.1 mAh·g^{-1} (corresponding to 2025.3 mAh·g^{-1} on the mass of phosphorus) at 425 mA·g^{-1} and 627.2 mAh·g^{-1} after 300 cycles with capacity retention of 77.4%. Additionally, high capacity was realized at 3400 mA·g^{-1} with reversible capacity of 480 mAh·g^{-1}. Also, the prepared red P/anthracite composite exhibited superior sodium storage properties for sodium-ion batteries.

Lithium-ion batteries (LIBs) are the dominating power sources in portable electronics and electric vehicles nowadays [1–7]. Graphite has been the choice of anode for LIBs since 1991 due to its stable electrochemical performance [8]. However, its low theoretical specific capacity (372 mAh·g^{-1}) becomes a limiting factor for further increasing the energy density of LIBs [9], and its low working potential (~ 0.1 V vs. Li^+/Li) makes graphite not ideal for use in fast-charging LIBs, since the potential would easily drop to 0 V (vs. Li^+/Li) and induce the deposition of metallic lithium under fast-charging condition [10]. Red phosphorus (red P) has many virtues as battery anode, including high theoretical capacity of 2596 mAh·g^{-1}, low cost, good chemical stability and reasonable lithiation potential (~ 0.7 V vs. Li^+/Li) [11, 12], which could help to avoid lithium metal plating during fast charging. However, red P suffers from poor electronic conductivity (1×10^{-14} S·cm^{-1}) and drastic volume variation (~ 300%) [13], which cause quick structural degradation during cycling and inferior electrochemical performance. Construction of carbon-based compositions could effectively improve electronic conductivity and buffer the volume change. Ball milling [14–17] and vaporization conversion [18] are two common methods for the fabrication of red P/carbon composites. Vaporization conversion approach takes advantage of low sublimation temperature of red P and red P can easily condense into the pore of carbon materials. On the other hand, using ball milling approach can avoid the formation of toxic white

Supplementary Information The online version contains supplementary material available at https://doi.org/10.1007/s12598-021-01949-0.

Y.-C. Tan, W.-W. Liu*, W.-Y. Wang, X.-X. Liu, J.-M. Du, Y.-M. Sun*
Wuhan National Laboratory for Optoelectronics, Huazhong University of Science and Technology, Wuhan 430074, China
e-mail: liuww0000@163.com

Y.-M. Sun
e-mail: yongmingsun@hust.edu.cn

phosphorus and is facile for large-scale fabrication. Various carbon materials including carbon black (CB) [19, 20], graphene [21, 22], carbon nanotubes (CNT) [23, 24], biomass driven carbon [25], porous carbon [26], and heteroatom doped carbon [27, 28] have been combined with phosphorus, and the as-fabricated composite materials often deliver high electronic conductivity and enhanced electrochemical performance [29–31]. However, the involved preparation process of these carbon materials or P/carbon composites was often complex and the cost was often high. Therefore, it is desirable to explore advanced phosphorus/carbon composites with superior electrochemical performance using facile and scalable approach in consideration of commercial application.

Coal is an abundant resource with low cost, which is usually used as fossil fuel. Lignite, bitumite and anthracite are three representative coals with different metamorphic grades. Among them, anthracite possesses the highest mass ratio of carbon content (89 wt% or higher), the lowest volatile content, and high electronic conductivity. Coal has been reported as the raw materials to synthesize various carbon materials as anodes served for LIBs [32–34] and SIBs [35–38]. Typically, coal was used as precursor to fabricate needle cokes or mesophase asphalt microspheres [38–40], which can be further graphitized into artificial graphite. Carbon materials with different oxygen contents (0.3 at%–2.9 at%) and defect concentrations were fabricated with coal pitch as precursor annealed from 400 °C to 1550 °C. The sample achieved after annealing at 800 °C delivered 263 $mAh{\cdot}g^{-1}$ at 40 $mA{\cdot}g^{-1}$ served as anode for SIBs [36]. The pyrolyzed anthracite achieved after 1200 °C treatment displayed the best electrochemical performance among samples obtained under different annealing temperatures from 1000 to 1400 °C. Also, the 1200 °C-pyrolyzed anthracite delivered the highest reversible capacity of 222 $mAh{\cdot}g^{-1}$ at 60 $mA{\cdot}g^{-1}$ and the best rate capability for electrochemical sodium ion storage [37].

Herein, we showed a red P/anthracite composite featuring red P embedded into micrometer-scale porous anthracite framework, which was fabricated through a ball milling approach. Meanwhile, high specific surface area and pore volume of anthracite made it suitable to serve as an efficient host material to confine red P within the structure and buffer its volume change during cycling. Red P and anthracite were kneaded up together to produce uniform red P/anthracite composite after ball milling. The strong interactions of P–C and P–O–C bonds ensured tight combination between the red P and anthracite. The red P/anthracite composite with 40 wt% red P showed stable cycling performance and superior rate capability for LIBs. It delivered a high reversible capacity of 810.1 $mAh{\cdot}g^{-1}$ at 425 $mA{\cdot}g^{-1}$ and a high capacity retention of 77.4% was achieved after 300 cycles. As the current density increased to 3400 $mA{\cdot}g^{-1}$, a reversible capacity of 480 $mAh{\cdot}g^{-1}$ was obtained, showing good rate capability. Also, good cycling stability was achieved for SIBs.

Figure 1a shows the schematic illustration of fabrication process for red P/anthracite composite. Micro-sized red P/anthracite composite was obtained featured with red P uniformly embedded into the anthracite by ball milling operation. Figure 1b compares X-ray diffraction (XRD) results of commercial anthracite, commercial red P and red P/anthracite composite. The red P presented three broad peaks at about 15°, 33° and 55° [27]. The anthracite exhibited two sharp peaks at about 26.6° and 43.6°, suggesting high carbonization degree of the anthracite. In XRD pattern of the red P/anthracite, two weak graphitic peaks could be observed, while the original broad peaks of red P disappeared, indicating the successful fabrication of red P/anthracite composite [22, 41]. Raman spectra for the red P/anthracite and the bare anthracite are shown in Fig. 1c. The intensity ratio of D band to G band (I_D/I_G) for the two samples was calculated to compare the structure change of carbon. The increased I_D/I_G value from 0.93 for the bare anthracite to 1.02 for the red P/anthracite suggested that the amorphous degree was enhanced and defective sites were generated due to the permeation of red P into anthracite matrix [26]. The red shift of D band from 1442 cm^{-1} for the bare anthracite to 1334 cm^{-1} for the red P/anthracite could be attributed to the electron transfer from red P to anthracite, indicating the formation of strong interaction between red P and anthracite [42, 43].

X-ray photoelectron spectroscopy (XPS) and Fourier transform infrared spectroscopy (FTIR) were performed to investigate the chemical composition and functional groups of the obtained materials. Figure 1d displays high-resolution P 2p spectra of commercial P and red P/anthracite composite. In the spectra of pristine red P, two peaks centered at 130.1 and 131 eV were referred to P $2p_{3/2}$ and P $2p_{1/2}$, respectively. In comparison, two new peaks located at 131.6 and 133.9 eV were found in the spectrum of the red P/anthracite, which were referred to P–C and P–O–C bonds [26, 44], respectively. Different from anthracite and red P, an obvious adsorption peak centered at 1008 cm^{-1} of red P/anthracite emerged in FTIR spectra, which suggested the formation of P–O–C bond [21, 24, 45] (Fig. 1e). Brunauer–Emmett–Teller (BET) was conducted to analyze the change of specific surface area and pore distribution of anthracite before and after ball milling, as shown in Fig. 1f, g. According to the results of N_2 adsorption/desorption measurement, the red P/anthracite composite showed much smaller specific surface area than bare anthracite (17.3 $m^2{\cdot}g^{-1}$ for the P/anthracite vs. 544.9 $m^2{\cdot}g^{-1}$ for the anthracite). The pore volume of the red P/anthracite composite was 0.14 $cm^3{\cdot}g^{-1}$, which was also much smaller than that of anthracite (0.40 $cm^3{\cdot}g^{-1}$). According to

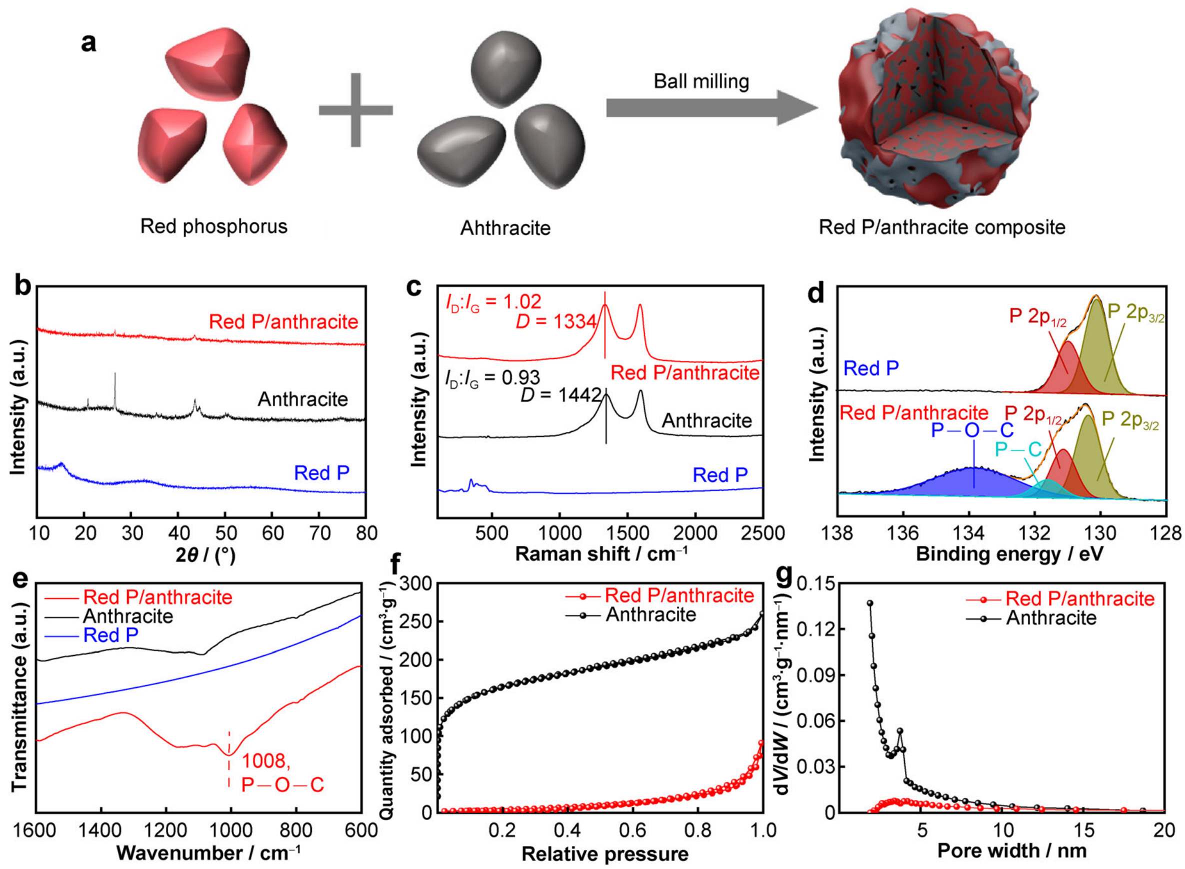

Fig. 1 **a** Schematic illustration of synthesis of red P/anthracite composite; **b** XRD patterns and **c** Raman spectroscopy of anthracite (after ball milling), red P and red P/anthracite composite; **d** XPS spectra of red P and red P/anthracite composite; **e** FTIR spectra of red P, anthracite and red P/anthracite composite; **f** N_2 adsorption/desorption isotherms and **g** pore distribution curves of anthracite and red P/anthracite composite

Barrett–Joyner–Halenda (BJH) pore size analysis of the anthracite, the average pore size of anthracite is ~ 4.1 nm. The significantly decreased specific surface area and pore volume indicated the successful filling of red P to the pores of anthracite [46]. All the results from Raman, FTIR, XPS and BET measurement confirmed the successful fabrication of red P/anthracite composite with chemical interaction between P and anthracite.

The morphology and microstructure of anthracite and P/anthracite were characterized using scanning electron microscopy (SEM) and transmission electron microscopy (TEM). In Fig. 2a, the anthracite particles showed irregular shape with micrometer-scale size. After ball milling, the red P and anthracite were kneaded together, and homogeneous particles of red P/anthracite in micrometer scale were obtained (Fig. 2b). TEM image and corresponding elemental mapping images of red P/anthracite are displayed in Fig. 2c–f. The results showed that P was filled into the interspace of anthracite and uniformly distributed over the entire composite. The anthracite with high specific surface area and pore volume not only can serve as efficient physical confinement for red P and buffer matrix for its volume change during the electrochemical reaction, but also can supply conductive pathway for electronic transport and enhanced the rate capability. Moreover, the close contact between red P and anthracite with P–C and P–O–C bonds can help to form a tight combination between red P and anthracite, which is beneficial for stable electrochemical cycling.

Figure 3 displays the electrochemical performance of red P/anthracite electrode for LIBs. Unless otherwise noted, the total weight of red P and anthracite was used to calculate the specific capacities. Figure 3a shows cyclic voltammetry (CV) curves of red P/anthracite composite at a scan rate of 0.1 $mV\cdot s^{-1}$ between 0.01 and 2.00 V (vs. Li/Li^+). Cathodic peaks were located at 1.0 and 0.5 V during initial lithiation process. The weak peak at ~ 1.0 V was attributed to the formation of the solid electrolyte interface (SEI). This broad peak disappeared in the subsequent cycles, as a reason of forming stable SEI film after initial cycle [27]. Cathodic peaks of subsequent two cycles were located at around ~ 0.37 and ~ 0.62 V, corresponding to

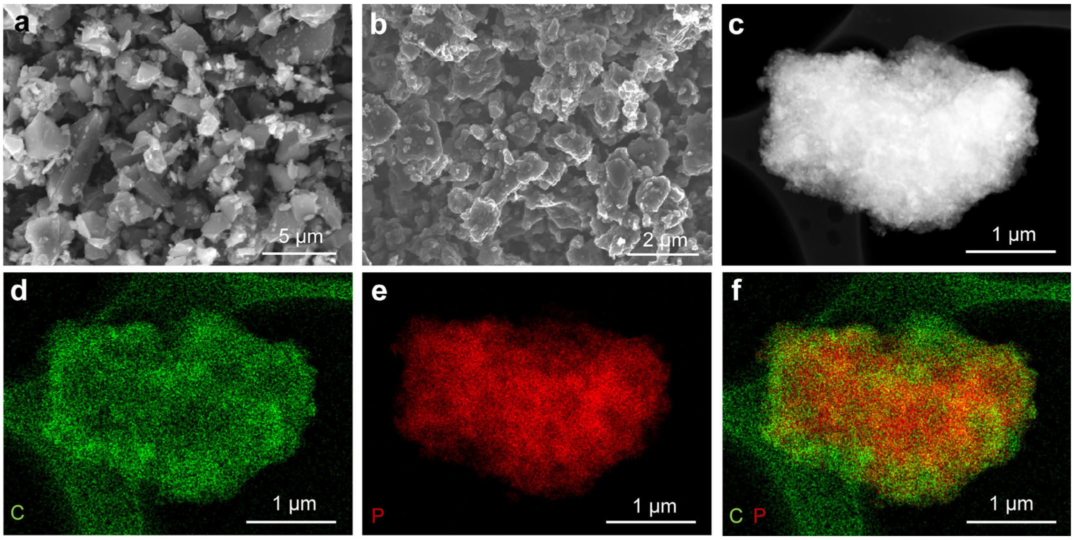

Fig. 2 SEM images of **a** anthracite and **b** red P/anthracite composite; **c** TEM image of red P/anthracite composite and corresponding elemental mapping images of **d** carbon, **e** phosphorus and **f** carbon and phosphorus elements

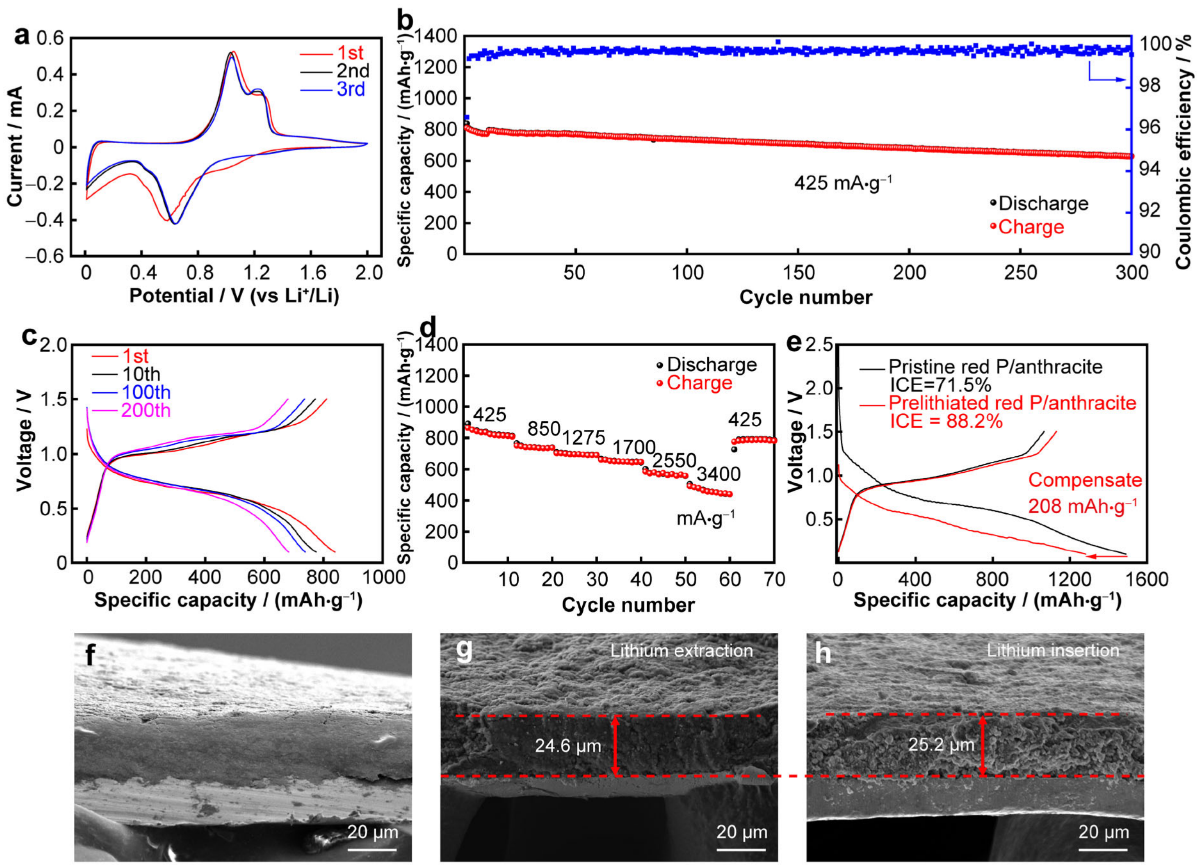

Fig. 3 Electrochemical performance of red P/anthracite composite for LIBs: **a** CV curves of red P/anthracite composite achieved at 0.1 $mV\cdot s^{-1}$; **b** galvanostatic cycling performance of red P/anthracite composite at 425 $mA\cdot g^{-1}$ and **c** voltage-capacity profiles of red P/anthracite composite for different cycles at 425 $mA\cdot g^{-1}$; **d** rate capability of red P/anthracite composite; **e** first-cycle voltage-capacity profiles of red P/anthracite composite electrodes without and with chemical prelithiation; **f** cross-sectional SEM image of red P/anthracite electrode before cycling; cross-sectional SEM images for 30th cycle at 425 $mA\cdot g^{-1}$ at **g** delithiation state and **h** lithiation state

the lithiation of red P. The corresponding anodic peaks were located at 1.1 and 1.3 V, corresponding to the delithiation of red P. The curves of the subsequent two cycles coincided well and displayed identical characteristic peaks, suggesting good electrochemical reversibility.

Figure 3b presents the cycling performance of red P/anthracite composite at 425 $mA\cdot g^{-1}$. After three activated cycles, the red P/anthracite electrode showed a high capacity of 810.1 $mAh\cdot g^{-1}$ (corresponding to 2025.3 $mAh\cdot g^{-1}$ for P). The red P/anthracite displayed capacity retention of 77.4% and average Coulombic efficiency of 99.77% for 300 cycles, presenting high electrochemical reversibility. The voltage-capacity profiles of the red P/anthracite composite at 1st, 10th, 100th and 200th cycles after three activation cycles are presented in Fig. 3c and these curves were highly overlapped, supporting the good electrochemical stability of the red P/anthracite.

The capacities of the red P/anthracite composite at various current densities are recorded in Fig. 3d. The composite electrode delivered high reversible capacities of 842.4, 742.4, 701.1, 653.9 and 580.4 $mAh\cdot g^{-1}$ at 425, 850, 1275, 1700, 2550 $mA\cdot g^{-1}$, respectively. Even at a high current density of 3400 $mA\cdot g^{-1}$, a high capacity of 480 $mAh\cdot g^{-1}$ was realized. Along with the current density went back to 425 $mA\cdot g^{-1}$ after tested at different current densities, a high capacity of 771.1 $mAh\cdot g^{-1}$ was still realized, which was close to the initial capacity achieved at 425 $mA\cdot g^{-1}$, showing good stability of the red P/anthracite electrode. It is noted that the capacity contributed by anthracite was negligible (Figs. S2, S3). The initial Coulombic efficiency of the red P/anthracite was moderately low, which would reduce the energy density of full batteries. To improve the initial Coulombic efficiency and compensate initial irreversible active lithium loss, the red P/anthracite electrode was chemically prelithiated using naphthalene solution [47–49] (see details in the experimental part). The initial Coulombic efficiency of the red P/anthracite was easily increased from 71.5% (the original electrode) to 88.2%, and 208 $mAh\cdot g^{-1}$ lithium ion capacity was compensated after prelithiation (Fig. 3e). What's important, the prelithiated red P/anthracite electrode did not have negative effect on cycling stability, displaying a high capacity retention of 75.4% after 250 cycles (Fig. S5). Such result indicated that the prelithiation process had no negative effect on the electrochemical cycling stability of the P/anthracite electrode.

Figure S6 shows the top view SEM image of the red P/anthracite electrode before and after cycling. It was observed that the red P/anthracite electrode maintained an intact structure without obvious fractures after 300 cycles, which was ascribed to its rational structure design. The cross-sectional SEM images of the red P/anthracite electrode before cycling and after 30 cycles were further compared (Fig. 3f–h). The thickness of the electrode showed only slightly increase from 24.6 (delithiation state) to 25.2 μm (lithiation state), indicating that the drastic volume expansion of phosphorus during the lithiation was effectively restrained by the anthracite matrix. The embedding structure of red P/anthracite composite guaranteed the tight connection between phosphorus and the anthracite matrix, leading to small electrode thickness variation and long-term cycling stability.

Electrochemical sodium storage properties of red P/anthracite electrodes were also investigated. Figure 4a shows CV curves of the red P/anthracite composite at 0.1 $mV\cdot s^{-1}$ (0.01–1.50 V). Irreversible broad peak at 0.75 V in the cathodic scan corresponded to the formation of SEI layer [21]. In the anodic scan, two sharp peaks around 0.54 and 0.65 V were assigned to the desodiation process and overlapped well in the next two cycles, indicating good electrochemical reversibility of the red P/anthracite composite for sodium-ion storage. After three activated cycles at 85 $mA\cdot g^{-1}$, charge capacity of the red P/anthracite electrode reached 692.3 $mAh\cdot g^{-1}$ at 170 $mA\cdot g^{-1}$ (Fig. 4b). After 150 cycles, the red P/anthracite electrode still exhibited a high capacity of 541.5$mAh\cdot g^{-1}$ with capacity retention of 78.2% (Fig. 4b). Figure 4c shows the voltage-capacity plots of red P/anthracite for different cycles. Only slight increase in voltage hysteresis was observed for the red P/anthracite on cycling, showing its high electrochemical reversibility. The rate capability of the red P/anthracite electrode is shown in Fig. 4d. Reversible capacities of 676.4, 652.2, 600.1, 534.5 and 428.1 $mAh\cdot g^{-1}$ were achieved at 170, 425, 850, 1700, 3400 $mA\cdot g^{-1}$, respectively.

In summary, a novel red P/anthracite composite was prepared via a simple ball milling approach, where amorphous red P was embedded in a porous anthracite framework. Owing to the homogeneous distribution of P in porous anthracite matrix with chemical binding (P–C and P–O–C bonds), the volume change of active P during the electrochemical reaction was relieved, and the integrity of the red P/anthracite was realized after cycling. Also, the anthracite provided abundant pathways for fast electronic transport, which afforded good rate capability. As a result, remarkable electrochemical performance was achieved for the red P/anthracite composite for both lithium-ion storage and sodium-ion storage, including high overall capacity (810.1 $mAh\cdot g^{-1}$ at 425 $mA\cdot g^{-1}$ for LIBs), good cycling stability (capacity retention of 77.4% for 300 cycles for LIBs) and rate capability (480 $mAh\cdot g^{-1}$ at 3400 $mA\cdot g^{-1}$ for LIBs). The low cost and scalable synthesis of such a red P/anthracite composite make it a competitive candidate as anode material for practical battery applications.

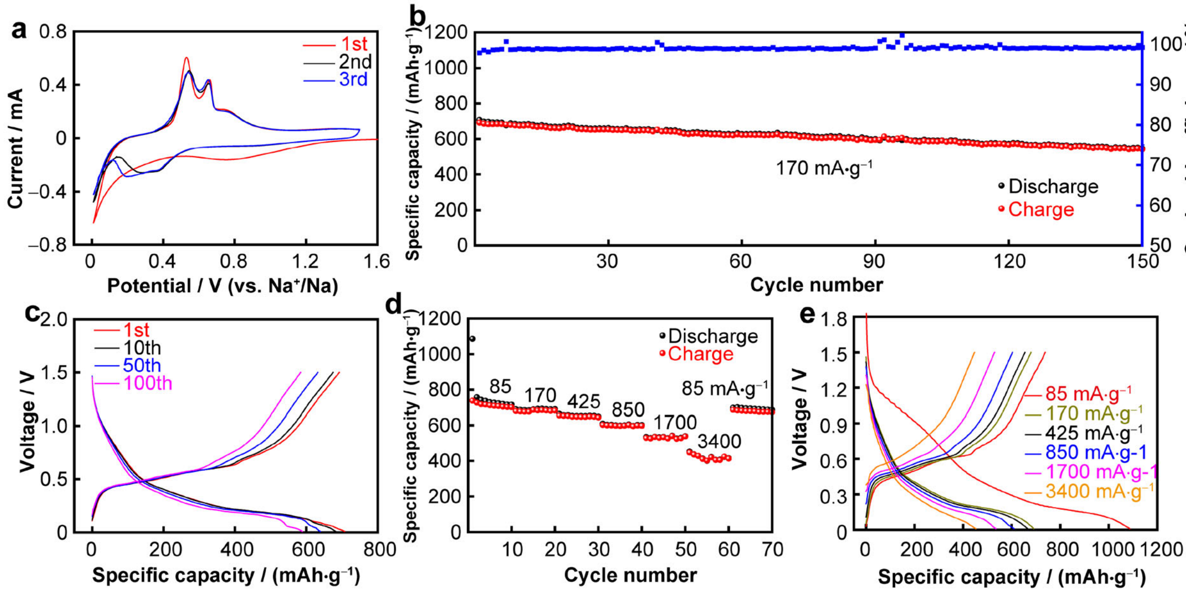

Fig. 4 Electrochemical performance of red P/anthracite as anode material for SIBs: **a** CV curves of red P/anthracite at 0.1 mV·s^{-1}; **b** galvanostatic cycling and **c** typical voltage-capacity profiles of red P/anthracite for different cycles at 425 mA·g^{-1}; **d** rate capability and **e** typical voltage-capacity profiles of red P/anthracite at different current densities

Acknowledgements This work was financially supported by the Innovation Fund of Wuhan National Laboratory for Optoelectronics and the National Natural Science Foundation of China (Nos. 51802105, 52072137 and 52002136). The authors would like to thank the Analytical and Testing Center of Huazhong University of Science and Technology as well as the Center for Nanoscale Characterization & Devices of Wuhan National Laboratory for Optoelectronics for providing the facilities to conduct the characterization.

Declarations

Conflicts of interests The authors declare that they have no conflict of interests.

References

[1] Tarascon JM, Armand M. Issues and challenges facing rechargeable lithium batteries. Nature. 2001;414(6861):359.
[2] Goodenough JB, Park KS. The Li-ion rechargeable battery: a perspective. J Am Chem Soc. 2013;135(4):1167.
[3. Dunn B, Kamath H, Tarascon JM. Electrical energy storage for the grid: a battery of choices. Science. 2011;334(6058):928.
[4] Lin DC, Liu YY, Cui Y. Reviving the lithium metal anode for high-energy batteries. Nat Nanotechnol. 2017;12(3):194.
[5] Tu SB, Su H, Sui D, He YW, Cheng MR, Bai PX, Zhang C, Sun PF, Wang CH, Jiang JX, Xu YH. Mesoporous carbon nanomaterials with tunable geometries and porous structures fabricated by a surface-induced assembly strategy. Energy Storage Mater. 2021;35:602.
[6] Li T, Liu H, Shi P, Zhang Q. Recent progress in carbon/lithium metal composite anode for safe lithium metal batteries. Rare Met. 2018;37(6):449.
[7] Chen TM, Jin Y, Lv HY, Yang AT, Liu MY, Chen B, Xie Y, Chen Q. Applications of lithium-ion batteries in grid-scale energy storage systems. Trans Tianjin Univ. 2020;26(3):208.
[8] Aurbach D, Markovsky B, Weissman I, Levi E, Ein-Eli Y. On the correlation between surface chemistry and performance of graphite negative electrodes for Li ion batteries. Electrochim Acta. 1999;45(1–2):67.
[9] Peled E, Menachem C, Bar Tow D, Melman A. Improved graphite anode for lithium ion batteries chemically: bonded solid electrolyte interface and nanochannel formation. J Electrochem Soc. 2019;143(1):L4.
[10] Sun Y, Wang L, Li YB, Li YZ, Lee HR, Pei A, He XM, Cui Y. Design of red phosphorus nanostructured electrode for fast-charging lithium-ion batteries with high energy density. Joule. 2019;3(4):1080.
[11] Sun J, Zheng GY, Lee HW, Liu N, Wang HT, Yao HB, Yang WS, Cui Y. Formation of stable phosphorus-carbon bond for enhanced performance in black phosphorus nanoparticle-graphite composite battery anodes. Nano Lett. 2014;14(8): 4573.
[12] Sun J, Lee HW, Pasta M, Yuan HT, Zheng GY, Sun YM, Li YZ, Cui Y. A phosphorene-graphene hybrid material as a high-capacity anode for sodium-ion batteries. Nat Nanotechnol. 2015; 10(11):980.
[13] Zhou JB, Liu XY, Cai WL, Zhu YC, Liang JW, Zhang KL, Lan Y, Jiang ZH, Wang GM, Qian YT. Wet-chemical synthesis of hollow red-phosphorus nanospheres with porous shells as anodes for high-performance lithium-ion and sodium-ion batteries. Adv Mater. 2017;29(29):1.
[14] Xu ZW, Zeng Y, Wang LY, Li N, Chen C, Li CY, Li J, Lv HM, Kuang LY, Tian X. Nanoconfined phosphorus film coating on interconnected carbon nanotubes as ultrastable anodes for lithium ion batteries. J Power Sour. 2017;356:18.
[15] Wang Y, Shi HT, Niu JR, Mai W, Liu LY, Xu ZW. Self-healing Sn_4P_3@hard carbon Co-storage anode for sodium-ion batteries. J Alloys Compd. 2021;851:156746.
[16] Liang ST, Li N, Wang HB, Jing ML, Wang W, Hu YL, Xu ZW, Liu LY, Li FY. "Rebar-reinforced concrete" carbon nanotubes/carbon black@phosphorus multilevel architecture from one-pot ball milling as anode materials. Ceram Int. 2019;45: 1331.

[17] Pei XY, Zhao MY, Li RX, Lu H, Yu RR, Xu ZW, Li DS, Tang YH, Xing WJ. Porous network carbon nanotubes/chitosan 3D printed composites based on ball milling for electromagnetic shielding. Compos Part A. 2021;145:106363.
[18] Liang ST, Pei XY, Jiang WW, Xu ZW, Wang W, Teng KY, Wang CH, Fu HJ, Zhang XX. Free-standing dual-network red phosphorus@porous multichannel carbon nanofibers/carbon nanotubes as a stable anode for lithium-ion batteries. Electrochim Acta. 2019;332:134696.
[19] Qian JF, Wu XY, Cao YL, Ai XP, Yang HX. High capacity and rate capability of amorphous phosphorus for sodium ion batteries. Angew Chem Int Ed. 2013;52(17):4633.
[20] Kim Y, Park Y, Choi A, Choi NS, Kim J, Lee J, Ryu JH, Oh SM, Lee KT. An amorphous red phosphorus/carbon composite as a promising anode material for sodium ion batteries. Adv Mater. 2013;25(22):3045.
[21] Song JX, Yu ZX, Gordin ML, Hu S, Yi R, Tang DH, Walter T, Regula M, Choi D, Li XL, Manivannan A, Wang DH. Chemically bonded phosphorus/graphene hybrid as a high performance anode for sodium-ion batteries. Nano Lett. 2014;14(11):6329.
[22] Yu ZX, Song JX, Gordin ML, Yi R, Tang DH, Wang DH. Phosphorus-graphene nanosheet hybrids as lithium-ion anode with exceptional high-temperature cycling stability. Adv Sci. 2015;2(1–2):1400020.
[23] Li WJ, Chou SL, Wang JZ, Liu HK, Dou SX. Simply mixed commercial red phosphorus and carbon nanotube composite with exceptionally reversible sodium-ion storage. Nano Lett. 2013;13(11):5480.
[24] Song JX, Yu ZX, Gordin ML, Li XL, Peng HS, Wang DH. Advanced sodium ion battery anode constructed via chemical bonding between phosphorus, carbon nanotube, and cross-linked polymer binder. ACS Nano. 2015;9(12):11933.
[25] Tian WF, Wang L, Huo KF, He XM. Red phosphorus filled biomass carbon as high-capacity and long-life anode for sodium-ion batteries. J Power Sourc. 2019;430:60.
[26] Liu BQ, Zhang Q, Li L, Jin ZS, Wang CG, Zhang LY, Su ZM. Encapsulating red phosphorus in ultralarge pore volume hierarchical porous carbon nanospheres for lithium/sodium-ion half/full batteries. ACS Nano. 2019;13(11):13513.
[27] Li WH, Hu SH, Luo XY, Li ZL, Sun XZ, Li MS, Liu FF, Yu Y. Confined amorphous red phosphorus in MOF-derived n-doped microporous carbon as a superior anode for sodium-ion battery. Adv Mater. 2017;29(16):1605820.
[28] Zhang C, Wang X, Liang QF, Liu XZ, Weng QH, Liu JW, Yang YJ, Dai ZH, Ding KJ, Bando Y, Tang J, Golberg D. Amorphous phosphorus/nitrogen-doped graphene paper for ultra-stable sodium-ion batteries. Nano Lett. 2016;16(3):2054.
[29] Yan ZH, Yang QW, Wang QH, Ma J. Nitrogen doped porous carbon as excellent dual anodes for Li and Na-ion batteries. Chin Chem Lett. 2020;31(2):583.
[30] Shi Y, Yu GH. Designing hierarchically nanostructured conductive polymer gels for electrochemical energy storage and conversion. Chem Mater. 2016;28(8):2466.
[31] Shi JD, Li XM, Cheng HY, Liu ZJ, Zhao LY, Yang TT, Dai ZH, Cheng ZG, Shi EZ, Yang L, Zhang Z, Cao AY, Zhu HW, Fang Y. Graphene reinforced carbon nanotube networks for wearable strain sensors. Adv Funct Mater. 2016;26(13):2078.
[32] Han L, Zhu X, Yang F, Liu Q, Jia XL. Eco-conversion of coal into a nonporous graphite for high-performance anodes of lithium-ion batteries. Powder Technol. 2021;382:40.
[33] Gao SS, Tang YK, Wang L, Liu L, Sun ZP, Wang S, Zhao HY, Kong LB, Jia DZ. Coal-based hierarchical porous carbon synthesized with a soluble salt self-assembly-assisted method for high performance supercapacitors and Li-ion batteries. ACS Sustain Chem Eng. 2018;6(3):3255.
[34] Xing BL, Zhang CT, Cao YJ, Huang GX, Liu QR, Zhang CX, Chen ZF, Yi GY, Chen LJ, Yu JL. Preparation of synthetic graphite from bituminous coal as anode materials for high performance lithium-ion batteries. Fuel Process Technol. 2018;172:162.
[35] Zhao HQ, Zhao D, Ye JQ, Wang PF, Chai MS, Li Z. Directional oxygen functionalization by defect in different metamorphic-grade coal-derived carbon materials for sodium storage. Energy Environ Mater. 2021;1.
[36] Qi YR, Lu YX, Ding FX, Zhang QQ, Li H, Huang XJ, Chen LQ, Hu YS. Slope-dominated carbon anode with high specific capacity and superior rate capability for high safety Na-ion batteries. Angew Chem Int Ed. 2019;58:4361.
[37] Li YM, Hu YS, Qi XG, Rong XH, Li H, Huang XJ, Chen LQ. Advanced sodium-ion batteries using superior low cost pyrolyzed anthracite anode: towards practical applications. Energy Storage Mater. 2016;5:191.
[38] Zhao D, Zhao HQ, Ye JQ, Song W, Miao SY, Shen HT, Zhao Y, Kang MM, Li Z. Oxygen functionalization boosted sodium adsorption-intercalation in coal based needle coke. Electrochim Acta. 2020;329:135127.
[39] Alvarez P, Díez N, Santamaría R, Blanco C, Menéndez R, Granda M. Novel coalbased precursors for cokes with highly oriented microstructures. Fuel. 2012;95:400.
[40] Yuan GM, Jin Z, Zuo XH, Xue Z, Yan F, Dong ZJ, Cong Y, Li XK. Effect of carbonaceous precursors on the structure of mesophase pitches and their derived cokes. Energy Fuel. 2018;32:8329.
[41] Jiao XX, Liu YY, Li B, Zhang WX, He C, Zhang CF, Yu ZX, Gao TY, Song JX. Amorphous phosphorus-carbon nanotube hybrid anode with ultralong cycle life and high-rate capability for lithium-ion batteries. Carbon. 2019;148:518.
[42] Marino C, Debenedetti A, Fraisse B, Favier F, Monconduit L. Activated-phosphorus as new electrode material for Li-ion batteries. Electrochem Commun. 2011;13(4):346.
[43] Qian JF, Qiao D, Ai XP, Cao YL, Yang HX. Reversible 3-Li storage reactions of amorphous phosphorus as high capacity and cycling-stable anodes for Li-ion batteries. Chem Commun. 2012;48(71):8931.
[44] Tao HC, Du SL, Zhang F, Xiong LY, Zhang YQ, Ma H, Yang XL. Achieving a high-performance carbon anode through the P-O bond for lithium-ion batteries. ACS Appl Mater Interfaces. 2018;10(40):34245.
[45] Sun J, Lee HW, Pasta M, Sun YM, Liu W, Li YB, Lee HR, Liu N, Cui Y. Carbothermic reduction synthesis of red phosphorus-filled 3D carbon material as a high-capacity anode for sodium ion batteries. Energy Storage Mater. 2016;4:130.
[46] Wang L, He XM, Li JJ, Sun WT, Gao J, Guo JW, Jiang CY. Nano-structured phosphorus composite as high-capacity anode materials for lithium batteries. Angew Chem Int Ed. 2012;51(36):9034.
[47] Liu XX, Tan YC, Liu TC, Wang WY, Li CH, Lu J, Sun YM. A simple electrode-level chemical presodiation route by solution spraying to improve the energy density of sodium ion batteries. Adv Funct Mater. 2019;29(50):1903795.
[48] Liu XX, Tan YC, Wang WY, Li CH, Seh ZW, Wang L, Sun YM. Conformal prelithiation nanoshell on $LiCoO_2$ enabling high-energy lithium-ion batteries. Nano Lett. 2020;20(6):4558.
[49] Liu XX, Liu TC, Wang R, Cai Z, Wang W, Yuan YF, Shahbazian-Yassar R, Li XC, Wang SR, Hu EY, Yang XQ, Xiao YG, Amine K, Lu J, Sun YM. Prelithiated Li-enriched gradient interphase toward practical high-energy NMC-silicon full cell. ACS Energy Lett. 2020;6(2):320.